Statistical Analysis of the Rotation Induced Decay of the Contrast in an Onboard Atom Interferometer

Benoît Kaczmarczuk, Joel Gomes Baptista, Sébastien Merlet, Leonid A Sidorenkov, Quentin Beaufils, Franck Pereira dos Santos

To cite this version:

Benoît Kaczmarczuk, Joel Gomes Baptista, Sébastien Merlet, Leonid A Sidorenkov, Quentin Beaufils, et al.. Statistical Analysis of the Rotation Induced Decay of the Contrast in an Onboard Atom Interferometer. IEEE Sensors Journal, 2025, 25 (16), pp.30889-30896. ⟨10.1109/JSEN.2025.3586409⟩. ⟨hal-05363851⟩

HAL Id: hal-05363851
https://hal.science/hal-05363851v1

Submitted on 13 Nov 2025

This article has been accepted for publication in IEEE Sensors Journal. This is the author's version which has not been fully edited and
content may change prior to final publication. Citation information: DOI 10.1109/JSEN.2025.3586409

Statistical analysis of the rotation induced decay of the contrast in an onboard atom interferometer

Benoît Kaczmarczuk, Joel Gomes Baptista, Sébastien Merlet, Leonid A. Sidorenkov, Quentin Beaufils,
Franck Pereira dos Santos

***Abstract*—We present a statistical analysis of the measurement noise of an atom interferometer under large phase and contrast noise caused by rotation fluctuations. The extraction of the standard deviation of the contrast fluctuations out of transition probability measurements allows us to determine the level of rotation noise applied to the onboard instrument. We include an experimental validation of the method.**

***Index Terms*—Atom Interferometry (AI), Inertial Sensors, Navigation**

I. INTRODUCTION

QUANTUM sensors based on cold-atom interferometry show performances that have or will have a significant impact in numerous fields including geophysics [1], [2] and geodesy [3]–[10], gravitational wave detection [11], tests of fundamental physics [12]–[16] and inertial navigation [17]. The variety of potential applications stimulated an effort to deploy this technology in diverse environments. Initially limited to quiet and controlled laboratory experiments [20], atom interferometers (AI) can be adapted to operate under critical conditions on ground [18], [19], onboard a vehicle [21], [22] (boat, aircraft) or in space [23].

Whether they are intended for gravity field recovery or inertial navigation, onboard applications are particularly demanding since they impose high levels of acceleration and angular velocity fluctuations. AIs have an inherent 2π phase ambiguity that limits their dynamic range and their ability to fully benefit from their high sensitivity in a noisy environments. Besides, they are sensitive to inertial effects such as Coriolis and centrifugal accelerations, which can cause measurement noise and reduce the contrast [24], limiting further their sensitivity. Methods to overcome those limitations have been developed, relying for instance on the hybridization with classical inertial sensors [19], [25].

Calibrations of the instrument in noisy environments rely on a statistical analysis of signal fluctuations, which allow to extract key parameters such as the contrast and the detection noise, which are assumed constant [26]. However, in many situations, the angular velocity of the instrument varies which leads to contrast fluctuations. In this article, we build on the previous approach and propose two different methods to extend the analysis of the statistical distribution of AI measurements to the case of large phase and contrast fluctuations caused by acceleration and rotation noise. In comparison to previous works, our methods allow to estimate both contrast and phase fluctuations with the same data set. The next section is dedicated to the description of these methods, and the last section presents experimental tests of the methods that were performed with a cold atom interferometer.

II. ANALYSIS OF THE TRANSITION PROBABILITY DISTRIBUTION

A. Context

We consider a three-pulse atom interferometer similar to the one described in [26]. The measured quantity at the output of the interferometer is the transition probability between the two ^{87}Rb hyperfine levels of the ground state:

$$\mathcal{P}_i = P_0 + \frac{C_i}{2}\cos(\phi_i) + \delta P_i \tag{1}$$

where P_0 is the offset of the interference fringes, C_i is the contrast defined as the fringe amplitude in transition probability and δP_i is an additive white Gaussian detection noise of standard deviation σ_P . Here the index i enumerates the successive measurements. The phase difference accumulated between the two arms of the interferometer ϕ_i is proportional to the acceleration along the measurement axis as well as rotation induced inertial pseudo-accelerations (Coriolis, centrifugal and Euler). In the presence of acceleration fluctuations, the variation of the phase between successive measurements can exceed 2π, causing an ambiguity on the corresponding transition probability. When the contrast is constant ($C_i = C_0$), an analysis of the transition probability distribution over a large number of measurements allows to demonstrate the

---

This work was supported in part by a government grant managed by the Agence Nationale de la Recherche under the Plan France 2030 with the reference ”ANR-22-PETQ-0005”, and by the European Defence Fund (EDF) under grant agreement 101103417 EDF-2021-DIS-RDIS-ADEQUADE.

Benoît Kaczmarczuk, Joël Gomes, Sebastien Merlet, Leonid Sidorenkov, Quentin Beaufils, Franck Pereira dos Santos are members of LTE, Observatoire de Paris, Université PSL, Sorbonne Université, Université de Lille, LNE, CNRS, 61 avenue de l'Observatoire, 75014 Paris, France.

This article has been accepted for publication in IEEE Sensors Journal. This is the author's version which has not been fully edited and content may change prior to final publication. Citation information: DOI 10.1109/JSEN.2025.3586409

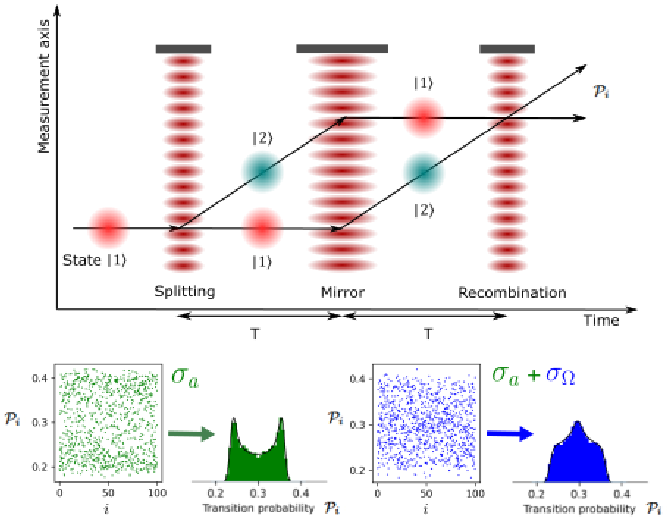

Fig. 1. In this work we consider a three pulse atom interferometer in a configuration analogous to an optical Mach-Zehnder interferometer. The atomic wavefunction undergoes a series of splitting, mirror, and recombination laser pulses. The transition probability between the two velocity states is measured after recombination. Under random acceleration phase, the trasition probability density function shows a characteristic shape (green histogram). Comparatively to previous works, we include the effect of angular velocity fluctuations (blue histogram).

coherence of the interferometer and estimate C_0, P_0 and σ_P [26]. Figure 2a shows the corresponding distribution, the Probability Density Function (PDF), for a random phase considered as a white noise of Gaussian standard deviation $\sigma_\phi \gg 2\pi$.

For onboard applications, rotations of the instrument can induce a loss of contrast via inhomogeneous Coriolis phase shifts : the finite temperature of the cloud is associated with a spread of velocity at the release, resulting in a phase inhomogeneity at the output of the interferometer. In the absence of a spatially resolved output state detection, this leads to a loss of contrast [28] that can be expressed as :

$$C_i = C_0 \exp\left(-2\sigma_v^2 k_{eff}^2 \Omega_i^2 T^4\right) \tag{2}$$

where Ω_i is the angular velocity in the plane perpendicular to the measurement direction, $\sigma_v = \sqrt{\frac{k_b \mathcal{T}}{m}}$ is the velocity dispersion for a temperature $\mathcal{T}$ and mass m, $k_{eff} = 4\pi/780$ nm is the effective wavevector of the interferometer beamsplitting pulse, and T is the interferometer separation time. A fluctuating angular velocity leads to a change of the PDF illustrated in figure 2b, c and d where Ω_i was modeled by a Gaussian white noise of increasing standard deviations σ_Ω.

B. First method : least squares fit

The first method we present is based on a least square fit of the histogram with four free parameters: P_0, C_0, σ_p and σ_Ω, respectively the central transition probability, the unperturbed contrast, the detection noise standard deviation (assumed here independent of $\mathcal{P}_i$) and the angular velocity noise standard deviation.

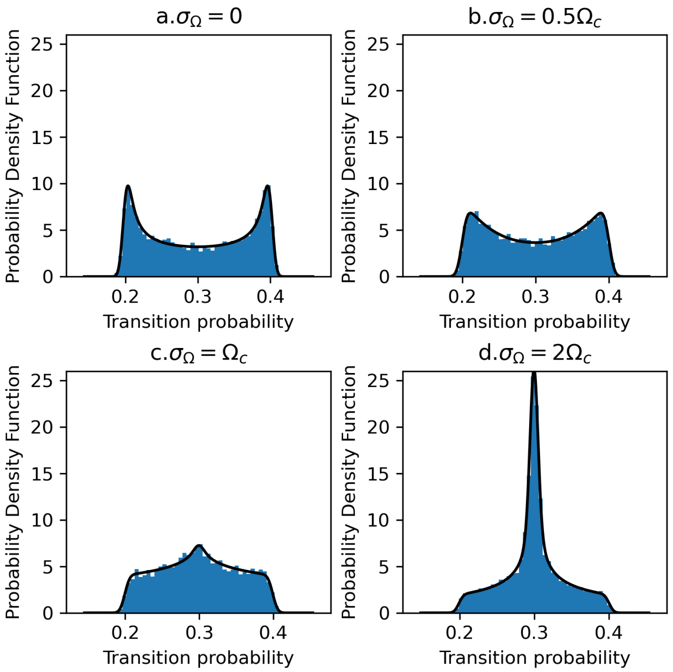

Fig. 2. Probability Density Functions (PDF) of the transition probability. $10\,000$ successive measurements were simulated with a random phase ($\sigma_\phi \gg 2\pi$) and with a random angular velocity fluctuations Ω_i of increasing standard deviations σ_Ω. a: $\sigma_\Omega = 0$, b: $\sigma_\Omega = 0.5\Omega_c$, c: $\sigma_\Omega = \Omega_c$, d: $\sigma_\Omega = 2\Omega_c$. $\sigma_P = 5\times10^{-3}$, $P_0 = 0.3$ and $C_0 = 0.2$. Ω_c is defined in equation (3). Solid lines are the results of the fits, following the procedure described in section II-B

We introduce the characteristic angular velocity Ω_c :

$$\Omega_c = \frac{1}{2\sigma_v k_{eff} T^2} \tag{3}$$

and express the contrast C_i as :

$$C_i = C_0 \exp\left(-\frac{1}{2}\frac{\Omega_i^2}{\Omega_c^2}\right) \tag{4}$$

The transition probability at each measurement i is thus given by :

$$\mathcal{P}_i = P_0 + \delta P_i^{det} + \frac{C_0}{2} e^{-\frac{1}{2}\frac{\Omega_i^2}{\Omega_c^2}} \cos(\phi_i) \tag{5}$$

That we rewrite as:

$$\mathcal{P}_i = P_0 + \delta P_i^{det} + \delta P^{phase}(\phi_i, \Omega_i) \tag{6}$$

The transition probability is a function of three random variables and the sum of two random functions. Its density function in the continuous domain can be written as the convolution of the density functions of P^{det} and P^{phase} :

$$f_{\mathcal{P}}(x) = (f_{\delta P^{det}} * f_{\delta P^{phase}})(x - P_0) \tag{7}$$

In order to adjust the histograms we use the cumulative distribution function $F_{\mathcal{P}}(x)$ defined as the integral of the density function :

$$F_{\mathcal{P}}(x) = (f_{\delta P^{det}} * F_{\delta P^{phase}})(x - P_0) \tag{8}$$

This article has been accepted for publication in IEEE Sensors Journal. This is the author's version which has not been fully edited and
content may change prior to final publication. Citation information: DOI 10.1109/JSEN.2025.3586409

We can express the PDF of the detection noise as a Gaussian distribution :

$$f_{\delta P^{det}}(x) = \frac{1}{\sigma_P\sqrt{2\pi}} e^{-\frac{1}{2}\frac{x^2}{\sigma_P^2}} \tag{9}$$

The detail of the calculation of the cumulative distribution function of δP^{phase} is given in the Appendix I. We obtain :

$$F_{\delta P^{phase}}(x) = \int_0^1 \frac{\Omega_c}{\sigma_\Omega} \frac{t^{\frac{\Omega_c^2}{\sigma_\Omega^2}}}{t\sqrt{-\pi\ln(t)}} \left(1 - \frac{1}{\pi}\cos^{-1}(\frac{2x}{C_0 t})\right) dt \tag{10}$$

Note that this function is only valid for a normal distribution of the random parameters. In order to adjust the histogram with this function, we perform a least-squares fit with a statistical approach :

- the histogram gives the measured probability for the transition probability $\mathcal{P}$ to be in the interval $[x_{j-1}, x_j]$ as N_j/N where N is the total number of measurements, and N_j is the number of measurements that fall in that interval.
- the cumulative distribution gives the theoretical probability for $\mathcal{P}$ to be in the interval $[x_{j-1}, x_j]$ as $F_{\mathcal{P}}(x_j) - F_{\mathcal{P}}(x_{j-1})$.

The best adjustment of the parameters $[\sigma_p, \sigma_\Omega, C_0, P_0]$ is the one that minimizes the quantity :

$$\sum_{j=1}^{N_{bin}} \left(F_{\mathcal{P}}(x_j) - F_{\mathcal{P}}(x_{j-1}) - \frac{N_j}{N}\right)^2 \tag{11}$$

When constructing the histograms, we adjust the binning according to the Terrell–Scott rule [27]. To ensure better convergence, we apply zero-padding equal to $2 \times 10\%$ of the data range before constructing the histogram :

$$\sqrt[3]{2N} \times (1 + 20\%) \approx 32 \tag{12}$$

C. Second method : equation of moments

The second method is based on the calculation of the moments of the distribution. The four unknown parameters (P_0, C_0, σ_p and σ_Ω) can be determined by a set of four equations based on the moments of different order. Since the distribution is an even function, only the even order moments are non null.

The first moment is the mean :

$$\mathbb{E}[\mathcal{P}] = P_0 \tag{13}$$

The second central moment, the variance, is given by:

$$\mathbb{E}[(\mathcal{P} - P_0)^2] = \sigma_p^2 + \frac{1}{8}\frac{C_0^2}{\sqrt{1 + 2\frac{\sigma_\Omega^2}{\Omega_c^2}}} \tag{14}$$

The fourth central moment, the kurtosis, is given by:

$$\mathbb{E}[(\mathcal{P} - P_0)^4] = 3\sigma_p^4 + \frac{3}{4}\frac{\sigma_p^2 C_0^2}{\sqrt{1 + 2\frac{\sigma_\Omega^2}{\Omega_c^2}}} + \frac{3}{128}\frac{C_0^4}{\sqrt{1 + 4\frac{\sigma_\Omega^2}{\Omega_c^2}}} \tag{15}$$

The sixth central moment, is given by:

$$\mathbb{E}[(\mathcal{P} - P_0)^6] = 15\sigma_p^6 + \frac{45}{8}\frac{\sigma_p^4 C_0^2}{\sqrt{1 + 2\frac{\sigma_\Omega^2}{\Omega_c^2}}} + \frac{45}{128}\frac{\sigma_p^2 C_0^4}{\sqrt{1 + 4\frac{\sigma_\Omega^2}{\Omega_c^2}}} + \frac{5}{1024}\frac{C_0^6}{\sqrt{1 + 6\frac{\sigma_\Omega^2}{\Omega_c^2}}} \tag{16}$$

We estimate $(\sigma_p, \sigma_\Omega, C_0, P_0)$ by equating theoretical moments with empirical moments [29] : $\mathbb{E}[\mathcal{P}] = \sum_i \mathcal{P}_i$; $\mathbb{E}[(\mathcal{P} - P_0)^2] = \sum_i (\mathcal{P}_i - P_0)^2$, $\mathbb{E}[(\mathcal{P} - P_0)^4] = \sum_i (\mathcal{P}_i - P_0)^4$ and $\mathbb{E}[(\mathcal{P} - P_0)^6] = \sum_i (\mathcal{P}_i - P_0)^6$. Combining these equations, we derive an equation with one unknown, σ_P, which we solve numerically, and with which we then calculate analytically the other unknowns (see details in the Supplementary Material).

D. Performance evaluation

Figure 2 shows transition probability histograms fitted with the method described in section II-B for different values of σ_Ω. Each histogram has been produced with the same values of σ_p, C_0, and P_0. All four parameters have been left free for the fit. The results are listed in table I, With uncertainties throughout the article defined at one σ.

To evaluate the ability of the adjustment procedure to retrieve and discriminate successfully σ_Ω from σ_P, we realized series of 100 measurement session simulations for different values of σ_Ω and σ_P. Each session consists in 10 000 successive simulated interferometer transition probability measurements. The 100 resulting histograms are fitted and the fit results are averaged and compared in figure 3 (left hand side) to the values used for the simulation of the histograms. Figure 4 displays the standard deviations of the fitted values.

TABLE I

RESULTS FROM THE FITS OF FIGURE 2. THE NUMBERS IN BRACKETS ARE THE VALUES USED FOR THE SIMULATION OF THE HISTOGRAMS. THE RESULTS OF THE FIT ARE LISTED ALONG WITH THE STANDARD DEVIATION ERRORS DEDUCED FROM THE COVARIANCE MATRICES.

	Results			
Data set (σ_Ω/Ω_c)	σ_Ω/Ω_c	σ_P (5×10^{-3})	P_0 (0.3)	C_0 (0.2)
a (0)	0.20 ±0.01	4.6×10^{-3} $\pm 0.2 \times 10^{-3}$	0.3001 ±0.0001	0.2035 ±0.0004
b (0.5)	0.51 ±0.01	5.0×10^{-3} $\pm 0.4 \times 10^{-3}$	0.3001 ±0.0003	0.2010 ±0.0006
c (1)	1.07 ±0.01	5.1×10^{-3} $\pm 0.6 \times 10^{-3}$	0.3001 ±0.0004	0.2006 ±0.0009
d (2)	1.97 ±0.01	5.1×10^{-3} $\pm 0.1 \times 10^{-3}$	0.2998 ±0.0001	0.2017 ±0.0014

These results can be compared to the results of the moments equation method, listed in table II and plotted on the right hand side of figure 3 and figure 4.

The two methods give qualitatively similar results. However, we identify three areas where the methods are less effective :

- The moments method shows a large dispersion and bias on the estimated σ_Ω for low detection noise ($\sigma_P <$

This article has been accepted for publication in IEEE Sensors Journal. This is the author's version which has not been fully edited and content may change prior to final publication. Citation information: DOI 10.1109/JSEN.2025.3586409

TABLE II

RESULTS OF THE MOMENTS METHOD. THE NUMBERS IN BRACKETS ARE THE VALUES USED FOR THE DATA GENERATION.

	Results			
Data set (σ_Ω/Ω_c)	σ_Ω/Ω_c	σ_P (5×10^{-3})	P_0 (0.3)	C_0 (0.2)
a (0)	0.28	1.5×10^{-3}	0.3011	0.2072
b (0.5)	0.51	4.8×10^{-3}	0.2995	0.2009
c (1)	0.95	4.9×10^{-3}	0.3002	0.2003
d (2)	2.00	3.8×10^{-3}	0.2992	0.2019

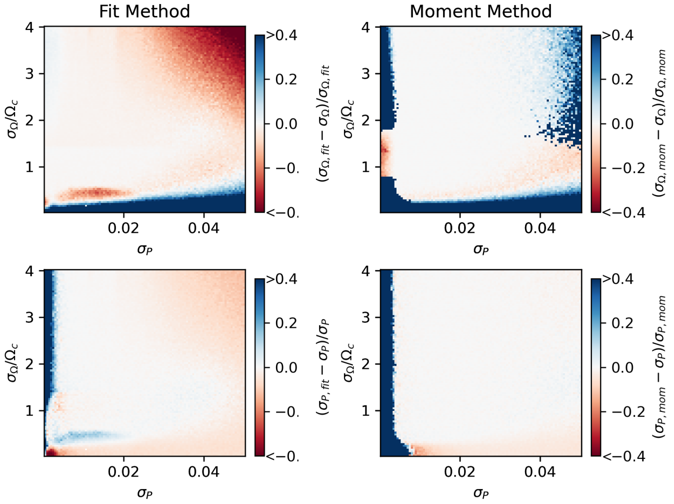

Fig. 3. Relative bias on the estimates of σ_P (top) and σ_Ω (bottom) as a function of σ_P on the y-axis and σ_Ω on the x-axis. Left: fits of the PDF, Right: method of moments. The bias is represented by color intensity. Each pixel is the average of 100 draws.

- 0.003). This is correlated with the absence of a real solution for σ_P (see supplementary material).
- Both methods show a large dispersion and bias on the estimated σ_Ω for low rotational noise ($\sigma_\Omega < 0.1$). This increase in dispersion is explained by the smaller variations in the PDF and in the moments with respect to σ_Ω, compared to the statistical fluctuations resulting from the finite number of draws. This increased dispersion also results in a bias. Indeed, σ_Ω being bound to positive values, the average of its fluctuating values scales with their dispersion.
- Both methods fail to discriminate σ_P from σ_Ω when both parameters are large.

According to Figure 5, the dispersion and biases for both methods decrease down to zero as the number of draws increases. We note though for the larger number of draws a resolved bias in the estimation of the detection noise using the fit method, which tends to be systematically underestimated. A convergence analysis indicates that this bias originates from the numerical method used to estimate the PDF.

III. EXPERIMENTAL TESTS

We tested experimentally our ability to evaluate the amplitude of the rotation velocity noise using the above methods with a cold-atom gravity gradiometer. The experimental setup, described in [30], consists of two cold atom clouds in free fall, vertically separated by a distance $d = 1$ m, and interrogated by the same pair of counter-propagating Bragg laser beams, thus realizing two simultaneous interferometers. Their common reference mirror is mounted on a tip-tilt platform and can rotate with a controlled constant angular velocity Ω_M during the interferometer sequence, which allows us to mimic a rotation of the whole system (see for example [24]). The phase of one interferometer is :

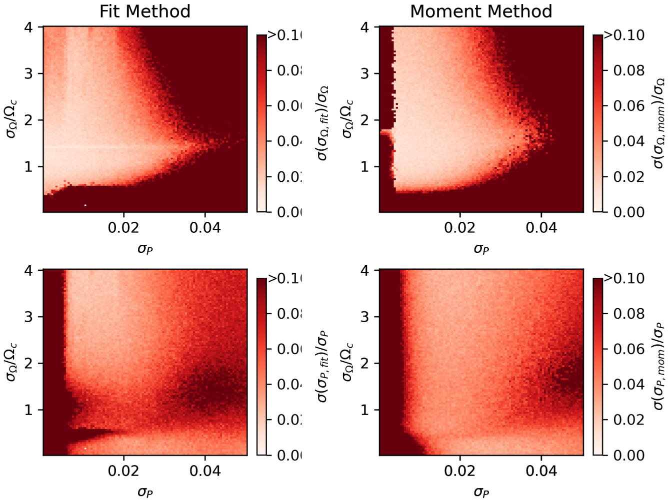

Fig. 4. Relative standard deviations on the estimates of σ_P (top) and σ_Ω (bottom) as a function of σ_P on the y-axis and σ_Ω on the x-axis. On the right are the results from the method of moments, and on the left are the results from the fits method. The relative standard deviation is represented by color intensity. Each pixel is the average of 100 successive simulations and the corresponding relative standard deviation is plotted as an error bar.

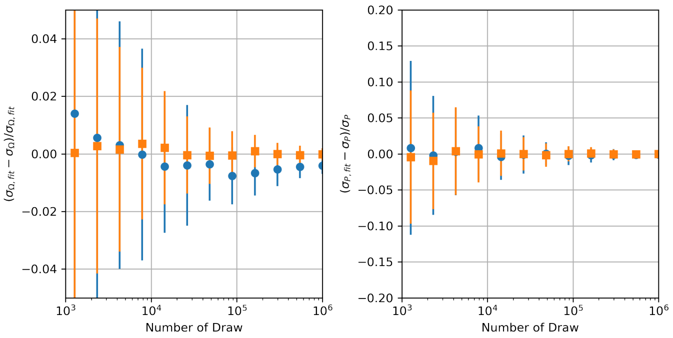

Fig. 5. Relative biases of the estimations of detection (on the left) and rotation velocity noise (on the right) using the method of moments (in orange) and the fit method (in blue), as a function of the number of draws. The bars represent the relative dispersion given by $\sigma(\sigma_{p,fit/mom})/\sigma_p$ for the detection noise estimation and $\sigma(\sigma_{\Omega,fit/mom})/\sigma_\Omega$ for the standard deviation of the rotational speed estimation. the parameters set for the simulation are $\sigma_\Omega = 2\Omega_c$, $\sigma_P = 0.02$ et $C_0 = 0.2$

$$\phi = k_{eff} a T^2 \tag{17}$$

where k_{eff} is the effective wave vector of the Bragg lasers, a is the acceleration of the atoms with respect to the reference mirror and T is the interrogation time.

For the interferometer duration used for this demonstration, of $2T = 120$ ms, mirror vibrations induced by ground seismic noise are not large enough to completely scramble the phase.

We thus artificially increase the phase noise by applying a random frequency difference between the Bragg lasers, so as to add a contribution to the interferometer phase spanning across several radians, ensuring that $\sigma_\phi \gg 2\pi$.

The transition probability is measured with a velocity-selective fluorescence detection system [31], where the atom clouds traverse a resonant laser light-sheet and their fluorescence is detected on a photodiode. The detection system has a limited spatial area that allows to measure only the atoms with a limited velocity in the direction of interest. This truncation of the detected atom cloud thus imposes an effective velocity distribution σ_{veff} smaller than the one deduced from the cloud temperature, and different for the two clouds falling from different heights. We calibrated the resulting contrast loss in the experiment as a function of Ω_M (figure 6). This allowed to determine experimentally the value of σ_{veff} and Ω_c for each cloud. We find $\Omega_c = 1.79 \pm 0.06$ mrad s^{-1} for the upper cloud and $\Omega_c = 1.34 \pm 0.03$ mrad s^{-1} for the lower cloud.

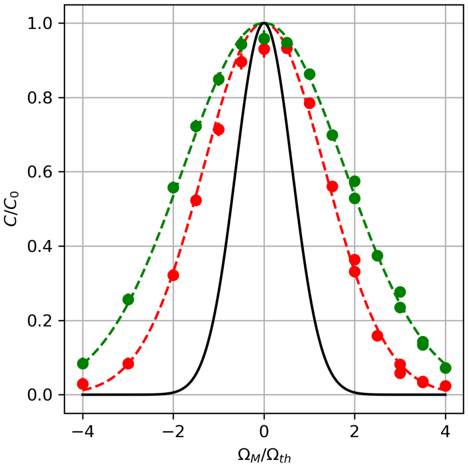

Fig. 6. Normalized contrast reduction due to the rotation of the interferometer versus the angular velocity of the mirror, for the upper (red) and lower (blue) atom clouds. Dashed lines are Gaussian fits yielding the values of Ω_c from which we can deduce σ_{veff}. The solid line is the expected contrast, calculated with equation 2 using the experimental value of the atomic cloud's temperature.

We then applied random fluctuations to the mirror's angular velocity Ω_M, with centered Gaussian distributions of standard deviations σ_Ω ranging between 0 and 2 mrad.s^{-1}, each to a set of ($\simeq$ 10 000) successive interferometer cycles. Typical results of the corresponding transition probabilities are displayed in Figure 7, for $\sigma_\Omega = 0$ and $\sigma_\Omega = 2$ mrad.s^{-1}. The resulting histograms were fitted using the procedure described in section II-B and the fit results (σ_Ω^{fit}, σ_P^{fit}, P^{fit}, C_0^{fit}) are plotted in figure 8, along with the results given by the moments method applied to the same data sets. We performed a linear fit of the extracted value of σ_Ω^{fit} as a function of the experimentally applied value σ_Ω and obtained $\sigma_\Omega^{fit}/\Omega_c = (0.908 \pm 0.008) \times \sigma_\Omega/\Omega_c$ for the lower cloud and $\sigma_\Omega^{fit}/\Omega_c = (0.976 \pm 0.009) \times \sigma_\Omega/\Omega_c$ for the upper cloud concerning the fit method ; and $\sigma_\Omega^{mom}/\Omega_c = (0.932 \pm 0.008) \times \sigma_\Omega/\Omega_c$ for the lower cloud and $\sigma_\Omega^{mom}/\Omega_c = (0.921 \pm 0.013) \times \sigma_\Omega/\Omega_c$ for the upper cloud concerning the moments method. We observe that the agreement is consistently close but smaller than one, which could be explained by an experimental underestimation of σ_{veff}.

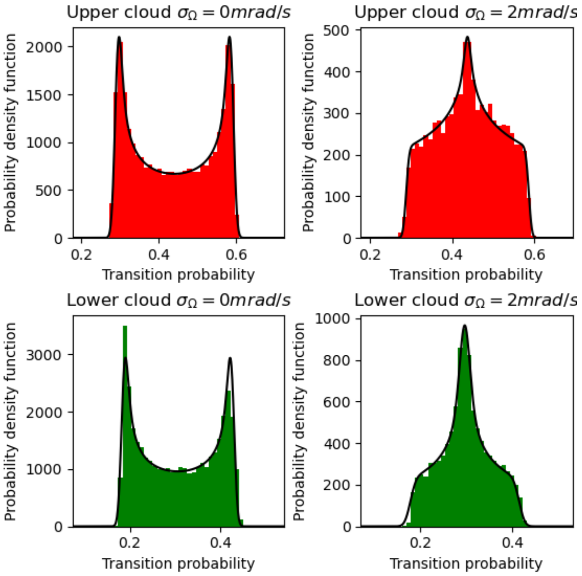

Fig. 7. Experimental PDFs with and without rotation noise, for the upper and lower atomic cloud. The solid lines are the results of the fit method. The number of measurements is 32 664 with $\sigma_\Omega = 0$ mrad s^{-1} and 9 077 with $\sigma_\Omega = 2$ mrad s^{-1}

The other parameters (σ_P, P_0, C_0) are not expected to change with the applied σ_Ω. The significant variations in the noise value σ_P, uncorrelated to σ_Ω, can be explained by variations in the number of detected atoms from one measurement sequence to an other.

IV. CONCLUSION

We presented two alternative statistical methods to calibrate a cold atom interferometer in a noisy environment. It allows to retrieve key instrumental parameters : the average transition probability P_0, the unperturbed contrast C_0, the transition probability standard deviation due to detection noise σ_P and the angular velocity standard deviation σ_Ω that causes contrast noise. Those methods are suited for onboard applications where the noise levels can be non-stationary. Regular noise calibrations allow to optimize instrumental parameters such as the interrogation time of the interferometer or the gain in a fringe-lock scheme [19]. In the future, tests of these techniques could be performed on various onboard atom interferometry data, when available, from future envisioned missions onboard satellites, boats, planes or research balloons. The implementation of the techniques on hybridized systems will be also studied.

The two methods were tested with simulated and experimental data. The numerical simulations demonstrated the effectiveness of the two methods to separate detection noise from rotation induced contrast noise, in a large region of parameters. The experimental tests showed a good agreement between the angular velocity dispersion σ_Ω applied to the mirror and the value obtained with both methods, further validating their relevance. Both methods require a large number of sample points to work effectively, which can limit their

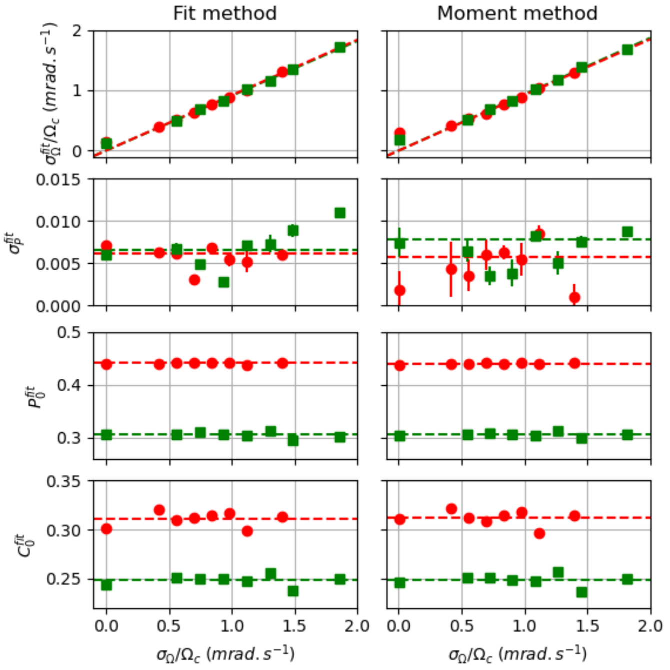

Fig. 8. Results of the fit method (left) and the moment method (right) on experimental results for the upper (red symbols) and lower clouds (green symbols).

effectiveness when the noise parameters vary too fast. Possible improvements would be optimizing computation speed for real time applications, or taking into account variations in the amplitude of the detection noise. Also, the study of the shape of the PDF could be used to characterize detection noise beyond the uniform case considered here, such as when operating at the quantum projection noise limit or below, via for instance the use of spin squeezing protocols [32].

APPENDIX I
EXPRESSION OF THE CUMULATIVE DISTRIBUTION FUNCTION

The expression for the loss of contrast induced by rotation in an interferometer for a constant angular velocity during one cycle is given by:

$$C = \exp\left(-\frac{2k_b\mathcal{T}}{m}k_{eff}^2(\Omega_x^2+\Omega_y^2)T^4\right) \qquad (18)$$

With:

- x and y the two directions transverse to the direction of the Raman pulses in z.
- Ω_x and Ω_y are the rotation velocities of the frame of reference in x and y.

If a rotation is applied only to the mirror with a rotation velocity Ω.

Introducing $\Omega_c = \frac{1}{2\sqrt{\frac{k_b\mathcal{T}}{m}}k_{eff}T^2}$, we get :

$$C = \exp\left(-\frac{1}{2}\frac{\Omega^2}{\Omega_c^2}\right) \qquad (19)$$

The transition probability finally writes as:

$$\mathcal{P} = P_0 + \delta P^{det} + \frac{C_0}{2}e^{-\frac{1}{2}\frac{\Omega^2}{\Omega_c^2}}\cos(\phi) \qquad (20)$$

We assume that Ω follows a centered standard distribution with standard deviation σ_Ω. The distribution function of the mirror rotation speed is given by:

$$f_\Omega(x) = \frac{1}{\sqrt{2\pi}\sigma_\Omega}\exp\left(-\frac{1}{2}\frac{x^2}{\sigma_\Omega^2}\right) \qquad (21)$$

We define the random variable X as:

$$X = \frac{C_0}{2}e^{-\frac{1}{2}\frac{\Omega^2}{\Omega_c^2}} = g_X(\Omega) \qquad (22)$$

with $g_X(x) = \frac{C_0}{2}e^{-\frac{1}{2}\frac{x^2}{\Omega_c^2}}$
Expressing the derivative of g

$$g_X'(x) = -\frac{1}{2}\frac{2x}{\Omega_c^2}\frac{C_0}{2}e^{-\frac{1}{2}\frac{x^2}{\Omega_c^2}} = -\frac{x}{\Omega_c^2}g_X(x) \qquad (23)$$

and introducing $g_{X,1}^{-1}(y)$ and $g_{X,2}^{-1}(y)$ the two solutions of the equation $g_X(x) = y$,

$$g_{X,1}^{-1}(y) = \Omega_c\sqrt{2\ln\left(\frac{C_0}{2y}\right)} \qquad (24)$$

$$g_{X,2}^{-1}(y) = -\Omega_c\sqrt{2\ln\left(\frac{C_0}{2y}\right)} \qquad (25)$$

The density function of the new random variable writes as:

$$\begin{aligned} f_X(y) &= \frac{f_\Omega(g_{X,1}^{-1}(y))}{\left|g_X'(g_{X,1}^{-1}(y))\right|} + \frac{f_\Omega(g_{X,2}^{-1}(y))}{\left|g_X'(g_{X,2}^{-1}(y))\right|} \\ &= \left|\frac{\Omega_c^2}{y\Omega_c\sqrt{2\ln\left(\frac{C_0}{2y}\right)}}\right| f_\Omega\left(\Omega_c\sqrt{2\ln\left(\frac{C_0}{2y}\right)}\right) \\ &+ \left|\frac{\Omega_c^2}{y\Omega_c\sqrt{2\ln\left(\frac{C_0}{2y}\right)}}\right| f_\Omega\left(-\Omega_c\sqrt{2\ln\left(\frac{C_0}{2y}\right)}\right) \qquad (26) \\ &= \frac{\Omega_c^2}{y\Omega_c\sqrt{2\ln\left(\frac{C_0}{2y}\right)}}\frac{1}{\sigma_\Omega\sqrt{2\pi}}e^{-\frac{\Omega_c^2}{\sigma_\Omega^2}\ln\left(\frac{C_0}{2y}\right)} \\ &+ \frac{\Omega_c^2}{y\Omega_c\sqrt{2\ln\left(\frac{C_0}{2y}\right)}}\frac{1}{\sigma_\Omega\sqrt{2\pi}}e^{-\frac{\Omega_c^2}{\sigma_\Omega^2}\ln\left(\frac{C_0}{2y}\right)} \end{aligned}$$

$$\begin{aligned} f_X(y) &= \frac{\Omega_c}{\sigma_\Omega}\frac{1}{y\sqrt{\pi\ln\left(\frac{C_0}{2y}\right)}}\exp\left(-\frac{\Omega_c^2}{\sigma_\Omega^2}\ln\left(\frac{C_0}{2y}\right)\right) \\ &= \frac{\Omega_c}{\sigma_\Omega}\frac{1}{y\sqrt{\pi\ln\left(\frac{C_0}{2y}\right)}}\left(\frac{C_0}{2y}\right)^{-\frac{\Omega_c^2}{\sigma_\Omega^2}} \end{aligned} \qquad (27)$$

Let Φ, the random variable associated with the interferometric phase for a totally random phase, that is to say that ϕ varies much more than 2π. The Cumulative distribution function of the cosine of ϕ is given by :

This article has been accepted for publication in IEEE Sensors Journal. This is the author's version which has not been fully edited and
content may change prior to final publication. Citation information: DOI 10.1109/JSEN.2025.3586409

$$F_{\cos\phi}(x) = 1 - \frac{1}{\pi}\cos^{-1}(x) \tag{28}$$

Let $\delta P^{phase} = X \times \cos\Phi$. With the product formula, the Cumulative distribution function of Y is :

$$\begin{aligned} F_{\delta P^{phase}}(x) &= \int_{-\infty}^{+\infty} f_X(t) F_{\cos\phi}(x/t)\, dt \\ &= \int_0^{\frac{C_0}{2}} \frac{\Omega_c}{\sigma_\Omega} \frac{1 - \frac{1}{\pi}\cos^{-1}\left(\frac{x}{t}\right)}{t\sqrt{\pi \ln\left(\frac{C_0}{2t}\right)}} \left(\frac{C_0}{2t}\right)^{-\frac{\Omega_c^2}{\sigma_\Omega^2}} dt \\ &= \int_0^1 \frac{\Omega_c}{\sigma_\Omega} \frac{1 - \frac{1}{\pi}\cos^{-1}\left(\frac{2x}{C_0 t}\right)}{t\sqrt{-\pi\ln(t)}} t^{\frac{\Omega_c^2}{\sigma_\Omega^2}}\, dt \end{aligned} \tag{29}$$

To obtain the transition probability, we add the random variable δP^{phase} to a normal random variable, centered on P_0, with standard deviation σ_p (the detection noise).

Finally, the Cumulative distribution function of the transition probability is the convolution between the Cumulative distribution function of δP^{phase} and the above mentioned normal distribution, of standard deviation σ_p, centered on P_0 :

$$F_{\mathcal{P}}(x) = (F_{\delta P^{phase}} * f_{\delta P^{det}})(x - P_0) \tag{30}$$

with : $f_{\delta P^{det}}(x) = \frac{1}{\sigma_P\sqrt{2\pi}} e^{-\frac{1}{2}\frac{x^2}{\sigma_P^2}}$

APPENDIX II
NUMERICAL RESOLUTION OF THE METHOD OF MOMENTS

The method of moments leads to a system of 4 equations with 4 unknowns, which can be reduced to finding the root of a degree-24 polynomial P. Due to the approximation of theoretical moments by empirical moments, it is possible that the polynomial has no root. In such a case, the root value is set to 0 :

$$\begin{aligned} F(\sigma_P) = &\left(-\frac{9E_2^2E_4}{4} + E_4^2\right) \\ &\left(-\frac{100E_2^2E_4}{81} + \frac{1600E_4^2}{729} - E_2E_6\right)^2 \\ &- \left(\frac{100E_2^2E_4^2}{27} - \frac{1600E_4^3}{729} - 2E_2^3E_6 + \frac{4E_2E_4E_6}{3}\right)^2 \end{aligned} \tag{31}$$

With :

$$\begin{cases} e_2 = \mathbb{E}[(P - P_0)^2] \\ e_4 = \mathbb{E}[(P - P_0)^4] \\ e_6 = \mathbb{E}[(P - P_0)^6] \end{cases} \tag{32}$$

And :

$$\begin{cases} E_2(\sigma_p) = (e_2 - \sigma_p^2)^2 \\ E_4(\sigma_p) = (e_4 - 6e_2\sigma_p^2 + 3\sigma_p^4)^2 \\ E_6(\sigma_p) = (e_6 - 15e_4\sigma_p^2 + 45e_2\sigma_p^4 - 15\sigma_p^6)^2 \end{cases} \tag{33}$$

Solving for the roots of the polynomial F we find the value of σ_P. P_0 is determined by averaging the data.

All that remains is to determine C_0 and σ_Ω using the two following equations:

$$e_2 = \sigma_p^2 + \frac{1}{8}\frac{C_0^2}{\sqrt{1 + 2\frac{\sigma_\Omega^2}{\Omega_c^2}}} \tag{34}$$

$$e_4 = 3\sigma_p^4 + \frac{3}{4}\frac{\sigma_p^2 C_0^2}{\sqrt{1 + 2\frac{\sigma_\Omega^2}{\Omega_c^2}}} + \frac{3}{128}\frac{C_0^4}{\sqrt{1 + 4\frac{\sigma_\Omega^2}{\Omega_c^2}}} \tag{35}$$

$$\sigma_\Omega = \Omega_c\sqrt{\frac{-\beta + \sqrt{\beta^2 - \beta}}{2}} \text{ with } \beta = 1 - \frac{4}{9}\frac{E_4(\sigma_p)}{E_2(\sigma_p)^2} \tag{36}$$

Finally, using (34), we find C_0 :

$$C_0 = \sqrt{8\sqrt{1 + 2\frac{\sigma_\Omega^2}{\Omega_c^2}} \cdot (e_2 - \sigma_p^2)} \tag{37}$$

The polynomial F in (31) has multiple roots, which we numerically determine for σ_P in the [0-0.01] range. However only one root is the actual solution to our problem. For each possible root σ_P, we calculate the corresponding C_0 and σ_Ω. To find the triplet (σ_P,C_0,σ_Ω) that is the solution to our problem, we select the triplet (σ_P,C_0,σ_Ω) which minimizes the quantity:

$$\begin{aligned} S(\sigma_P, C_0, \sigma_\Omega) = &\left(\mathbb{E}[(\mathcal{P} - P_0)^2] - \sum_i (\mathcal{P}_i - P_0)^2\right)^2 \\ &+ \left(\sqrt{\mathbb{E}[(\mathcal{P} - P_0)^4]} - \sqrt{\sum_i (\mathcal{P}_i - P_0)^4}\right)^2 \\ &+ \left(\sqrt[3]{\mathbb{E}[(\mathcal{P} - P_0)^6]} - \sqrt[3]{\sum_i (\mathcal{P}_i - P_0)^6}\right)^2 \end{aligned} \tag{38}$$

Equation (36) imposes: $0 < \beta^2 - \beta$ which, after calculation, gives: $9E_2(\sigma_p)^2 < 4E_4(\sigma_p)$. The estimation of the theoretical moments by the empirical moments may lead to a violation of this condition. In such a case, we consider: $\sigma_\Omega = \Omega_c\sqrt{\frac{-\beta}{2}}$. If this is not sufficient, then $\sigma_\Omega = 0$. As for the equation (37), it is necessary that $e_2 - \sigma_p^2 < 0$. If this is not the case, we set arbitrarily $C_0 = 0$.

REFERENCES

[1] L. Antoni-Micollier *et al.*, "Detecting volcano-related underground mass changes with a quantum gravimeter," *Geophys. Res. Lett.* 49, 10.1029/2022gl097814, 2022.

[2] B. Stray *et al.*, "Quantum sensing for gravity cartography," *Nature* 602, 590, 2022.

[3] M. Michel *et al.*, "The AQG-B Absolute Quantum Gravimeter: A Promising sensor for Volcano Monitoring," *IEEE Instrum. Meas. Mag*, vol. 23, no. 6, pp. 17-10, 2024.

[4] O. Carraz *et al.* "A Spaceborne Gravity Gradiometer Concept Based on Cold Atom Interferometers for Measuring Earth's Gravity Field," *Microgravity Science and Technology* 26, 139, 2014.

[5] P. Abrikosov *et al.*, "Impact of a novel hybrid accelerometer on satellite gravimetry performances," *Advances in Space Research.*, vol. 63, no. 10, pp. 3235-3248, 2019.

This article has been accepted for publication in IEEE Sensors Journal. This is the author's version which has not been fully edited and content may change prior to final publication. Citation information: DOI 10.1109/JSEN.2025.3586409

[6] N. Zahzam *et al.*, ”Hybrid Electrostatic - Atomic Accelerometer for Future Space Gravity Missions,” *Remote Sensing* Vol. 14, Page 3273, 2022.

[7] F. Migliaccio *et al.*, ”MOCASS: A Satellite Mission Concept Using Cold Atom Interferometry for Measuring the Earth Gravity Field,” *Surveys in Geophysics 2019 40:5*, vol. 40, pages 1029-1053, 2019.

[8] A. Trimeche *et al.*, ”Concept study and preliminary design of a cold atom interferometer for space gravity gradiometry”, *Class. Quantum Grav.* , 36, 215004, 2019.

[9] T. Lévèque *et al.* ”Gravity field mapping using laser-coupled quantum accelerometers in space, *Journal of Geodesy*, 95:1, 2021.

[10] A. HosseiniArani *et al., “*Advances in Atom Interferometry and their Impacts on the Performance of Quantum Accelerometers On-board Future Satellite Gravity Missions,” *Advances in Space Research*, vol. 74, no. 7, pp. 3186-3200, 2024.

[11] S. Dimopoulos *et al., “*Atomic gravitational wave interferometric sensor,” *Phys. Rev. D*, vol. 78, no. 12, pp. 122002, 2008.

[12] P. Haslinger *et al., “*Attractive force on atoms due to blackbody radiation,” *Nature Physics*, vol. 14, no. 3, pp. 257-260, 2018.

[13] C. Struckmann *et al., “*Platform and environment requirements of a satellite quantum test of the weak equivalence principle at the 10^{-17} level,” *Phys. Rev. D*, vol. 109, no. 6, pp. 064010, 2024.

[14] L. Morel *et al., “*Determination of the fine-structure constant with an accuracy of 81 parts per trillion,” *Nature*, vol. 588, no. 7836, pp. 61-65, 2020.

[15] Y. Balland *et al., “*Quectonewton local force sensor,” *Phys. Rev. Lett.*, vol. 133, no. 11, pp. 113403, 2024.

[16] G. Tino, “Testing gravity with cold atom interferometry: results and prospects,” *TQuantum Sci. Technol*, vol. 6, no. 2, pp. 024014, 2024.

[17] P. Cheiney *et al., “*Navigation-Compatible Hybrid Quantum Accelerometer Using a Kalman Filter,” *Phys. Rev. Applied*, vol. 10, no. 3, pp. 034030, 2018.

[18] L. Antoni-Micollier *et al., “*Absolute Quentum Gravimeters and Gradiometers for Field Measurement,” *IEEE Instrum. Meas. Mag*, vol. 27, no. 6, pp. 4-10, 2024.

[19] S. Merlet *et al., “*Operating an atom interferometer beyond its linear range,” *Metrologia*, vol. 46, no. 1, pp. 87-94, 2009.

[20] S. Merlet *et al., “*Calibration of a superconducting gravimeter with an absolute atom gravimeter,” *Journal of Geodesy*, vol. 95, no. 5, pp. 62, 2021.

[21] Y. Bidel *et al., “*Absolute marine gravimetry with matter-wave interferometry,” *Nature Communications*, vol. 9, no. 1, 2018.

[22] Y. Bidel *et al., “*Absolute airborne gravimetry with a cold atom sensor,” *Journal of Geodesy*, vol. 94, no. 2, pp. 20, 2020.

[23] Q. Beaufils *et al., “*Rotation related systematic effects in a cold atom interferometer onboard a Nadir pointing satellite,” *npj Microgravity*, vol. 9, no. 1, pp. 1-6, 2023.

[24] S.-Y. Lan *et al., “*Influence of the Coriolis Force in Atom Interferometry,” *Phys. Rev. Lett.*, vol. 108, no. 9, pp. 090402, 2012.

[25] J. Lautier *et al., “*Hybridizing matter-wave and classical accelerometers,” *Appl. Phys. Lett.*, vol. 105, pp. 144102, 2014.

[26] R. Geiger *et al.* ”Detecting inertial effects with airborne matter-wave interferometry,” *Nat Commun* 2, 474 (2011).

[27] G. R. Terrell *et al.*”Oversmoothed Non para metric Density Estimates,” *Journal of the American Statistical Association* 80, 389 (1985) pp. 209-214

[28] A. Roura *et al.* ”Overcoming loss of contrast in atom interferometry due to gravity gradients,” *New Journal of Physics* 16, 12, pp. 123012

[29] G. Casella *et al.* ”Statistical Inference,” *Duxbury Thomson learning* Second Edition, pp. 313

[30] R. Caldani *et al., “*Simultaneous accurate determination of both gravity and its vertical gradient,” *Phys. Rev. A*, vol. 99, no. 3, pp. 033601, 2019.

[31] R. Piccon *et al., “*Separating the output ports of a Bragg interferometer via velocity selective transport,” *Phys. Rev. A*, vol. 106, no. 1, pp. 013303, 2022.

[32] M. Riedel *et al., “*Atom-chip-based generation of entanglement for quantum metrology ,” *Nature*, vol. 464, 1170–1173, 2010.